Assessment of bone tissue mineralization by conventional x-ray microcomputed tomography: Comparison with synchrotron radiation microcomputed tomography and ash measurements

G. J. Kazakia,[a] A. J. Burghardt, S. Cheung, and S. Majumdar
Musculoskeletal and Quantitative Imaging Research Group, Department of Radiology, University of California, San Francisco, California 94158

(Received 8 November 2007; revised 21 March 2008; accepted for publication 19 April 2008; published 19 June 2008)

Assessment of bone tissue mineral density (TMD) may provide information critical to the understanding of mineralization processes and bone biomechanics. High-resolution three-dimensional assessment of TMD has recently been demonstrated using synchrotron radiation microcomputed tomography (SRμCT); however, this imaging modality is relatively inaccessible due to the scarcity of SR facilities. Conventional desktop μCT systems are widely available and have been used extensively to assess bone microarchitecture. However, the polychromatic source and cone-shaped beam geometry complicate assessment of TMD by conventional μCT. The goal of this study was to evaluate μCT-based measurement of degree and distribution of tissue mineralization in a quantitative, spatially resolved manner. Specifically, μCT measures of bone mineral content (BMC) and TMD were compared to those obtained by SRμCT and gravimetric methods. Cylinders of trabecular bone were machined from human femoral heads ($n=5$), vertebrae ($n=5$), and proximal tibiae ($n=4$). Cylinders were imaged in saline on a polychromatic μCT system at an isotropic voxel size of 8 μm. Volumes were reconstructed using beam hardening correction algorithms based on hydroxyapatite (HA)-resin wedge phantoms of 200 and 1200 mg HA/cm^3. SRμCT imaging was performed at an isotropic voxel size of 7.50 μm at the National Synchrotron Light Source. Attenuation values were converted to HA concentration using a linear regression derived by imaging a calibration phantom. Architecture and mineralization parameters were calculated from the image data. Specimens were processed using gravimetric methods to determine ash mass and density. μCT-based BMC values were not affected by altering the beam hardening correction. Volume-averaged TMD values calculated by the two corrections were significantly different ($p=0.008$) in high volume fraction specimens only, with the 1200 mg HA/cm^3 correction resulting in a 4.7% higher TMD value. μCT and SRμCT provided significantly different measurements of both BMC and TMD ($p<0.05$). In high volume fraction specimens, μCT with 1200 mg HA/cm^3 correction resulted in BMC and TMD values 16.7% and 15.0% lower, respectively, than SRμCT values. In low volume fraction specimens, μCT with 1200 mg HA/cm^3 correction resulted in BMC and TMD values 12.8% and 12.9% lower, respectively, than SRμCT values. μCT and SRμCT values were well-correlated when volume fraction groups were considered individually (BMC $R^2=0.97-1.00$; TMD $R^2=0.78-0.99$). Ash mass and density were higher than the SRμCT equivalents by 8.6% in high volume fraction specimens and 10.9% in low volume fraction specimens ($p<0.05$). BMC values calculated by tomography were highly correlated with ash mass (ash versus μCT $R^2=0.96-1.00$; ash versus SRμCT $R^2=0.99-1.00$). TMD values calculated by tomography were moderately correlated with ash density (ash versus μCT $R^2=0.64-0.72$; ash versus SRμCT $R^2=0.64$). Spatially resolved comparisons highlighted substantial geometric nonuniformity in the μCT data, which were reduced (but not eliminated) using the 1200 mg HA/cm^3 beam hardening correction, and did not exist in the SRμCT data. This study represents the first quantitative comparison of μCT mineralization evaluation against SRμCT and gravimetry. Our results indicate that μCT mineralization measures are underestimated but well-correlated with SRμCT and gravimetric data, particularly when volume fraction groups are considered individually. [DOI: 10.1118/1.2924210]

Key words: computed tomography, synchrotron radiation, bone tissue, mineralization, beam hardening

I. INTRODUCTION

Bone strength is influenced by many complex factors. Bone mineral density (BMD) assessed by dual x-ray absorptiometry is considered a surrogate measure for determining fracture risk, but does not entirely predict fracture or adequately assess therapeutic interventions. Recently, the importance of trabecular microarchitecture in determining bone strength

has been brought to the attention of the clinical community.[1,2] Improved predictions of biomechanical properties have been found as a result of including measures of trabecular bone structure.[3–5] By including compositional measures—e.g., degree and distribution of mineralization—even more powerful predictions of fracture risk may be possible.

Degree of mineralization of bone or tissue mineral density (TMD) is known to influence tissue-level mechanical properties.[6] Increased mineralization is associated with greater amounts of tissue damage,[7] and hypermineralized sites present localized sites for crack initiation.[8] The distribution of mineralization within bone tissue may also have an effect on tissue properties.[9,10] Thus, high-resolution three-dimensional (3D) quantification of tissue mineralization may provide information critical to the understanding of bone biomechanics and to the assessment of bone strength. Additionally, tissue engineering efforts as well as studies of mineralization mechanics would profit from the ability to image mineralization in a nondestructive, spatially resolved manner.

Common techniques for mineral evaluation include ashing,[11] microradiography,[12] backscattered electron microscopy,[13] nanoindentation,[14] and Fourier-transform infrared spectroscopy.[15] However, each of these techniques is destructive and none provide 3D information.

Three-dimensional spatially resolved assessment of TMD has recently been demonstrated using synchrotron radiation microcomputed tomography (SRμCT).[16,17] The monoenergetic, high flux, parallel beam used in SRμCT provides high spatial resolution, high signal-to-noise ratio, and accurate attenuation measurement, thus rendering SRμCT an appropriate gold standard for 3D TMD evaluation. However, SRμCT studies are inaccessible to many researchers due to the scarcity of SR facilities.

Conventional desktop μCT systems are widely available and have been used extensively to assess bone microarchitecture. Conventional μCT has been shown to provide accurate measures of architecture in trabecular bone as compared to SRμCT.[18] However, the polychromatic source and cone-shaped beam geometry complicate the assessment of TMD. Beam hardening effects resulting from the preferential attenuation of low energies from the polychromatic source lead to geometric nonuniformities in signal and a nonlinear relationship between attenuation and material density. Beam hardening correction algorithms have been introduced to overcome this limitation and have provided measurable improvements in attenuation linearity.[19] While qualitative comparisons of conventional and synchrotron radiation mineralization images have been made,[20,21] quantitative spatially resolved comparisons have not been performed.

The goal of this study was to evaluate μCT-based measurement of degree and distribution of bone mineralization in a quantitative, spatially resolved manner. Conventional μCT mineralization measurements were compared to those performed by SRμCT, the gold standard for 3D spatially resolved mineralization analysis, and by gravimetric methods (ashing), the standard for volume-averaged bone tissue measurements. Specifically, our objectives were to: (1) Compare μCT measurements of bone mineral content (BMC) and volume-averaged TMD to those derived by SRμCT and by gravimetric measurements and (2) compare μCT assessment of mineral distribution to that measured by SRμCT. To make spatially resolved comparisons, mineralization was evaluated as a function of distance from a trabecular surface. Architectural parameters determined by the two imaging techniques were also compared for completeness.

II. MATERIALS AND METHODS

II.A. Specimen preparation

UCSF Committee for Human Research approval was granted for this work. Femoral head specimens were surgically excised during hip arthroplasty procedures at UCSF. Vertebrae and tibiae were harvested from human cadavers (National Disease Research Interchange, Philadelphia, PA). Each specimen was taken from a unique donor. Cylinders of trabecular bone (8 mm diameter, 4 mm length) were machined from the femoral head (FEM, $n=5$), vertebral body (VERT, $n=5$), and proximal tibia (TIB, $n=4$). The specimens were completely cleaned of marrow using a water jet with sonicator agitation and detergent washes as necessary (1%, Tergazyme, Alconox, Inc.). No further chemical defatting was necessary to remove marrow. Specimens were stored at −20 °C when not being processed.

II.B. Conventional polychromatic μCT imaging

In preparation for imaging, each specimen was placed in an acrylic holder, submerged in saline, and vacuum degassed to remove any air bubbles trapped in the pore spaces. The cylinders were imaged while still submerged in saline on a conventional polychromatic μCT system (μCT 40 Scanco Medical AG., Bruttisellen, Switzerland). This device consists of an x-ray source producing a narrow-angle cone beam, a 0.5 mm thick aluminum filter plate to eliminate the lowest energies from the beam, a cesium iodide scintillator, and a 12 bit charge coupled device (CCD) detector (2048 $\times$64 pixels). A previous generation of this scanner has been described in detail.[22] Imaging was performed at a voxel size of 8 μm (isotropic) with a source potential of 70 kV and tube current of 114 μA. Each scan consisted of 2000 projections over 360 deg, with the sample rotated in equiangular steps about its longitudinal axis. For each projection, sampling occurred over an integration time of 250 ms and two images were averaged to reduce the effects of noise. Dark current and raw beam measurements were made once at the beginning of each scan. Scanning time was 11–12 h per specimen. Three-dimensional data sets were reconstructed using a cone beam approximation.[23] Attenuation values were converted to hydroxyapatite (HA) concentration using a linear regression derived by imaging a calibration phantom containing rods of HA-resin mixtures (0, 100, 200, 400, and 800 mg HA/cm^3).

To minimize the influence of specimen geometry on reconstructed linear attenuation values, a voltage- and scanner-specific beam hardening correction is generally implemented by users of this device. To create the beam hardening correction factor, a step wedge phantom composed of a HA-resin mixture (200 mg HA/cm^3) was imaged at the appropriate source voltage (70 kV) at a time-point previous to this experiment. This concentration was originally chosen by the manufacturer as a reasonable approximation of apparent level mineral density (averaged over the bulk sample volume) for trabecular bone specimens or whole bone samples from small animals. The x-ray intensity at each width of the wedge (I) and the unobstructed reference intensity (I_0) were measured. A polynomial was then fit to the $\ln(I_0/I)$ versus thickness data. The deviation of this polynomial from linearity indicates the degree of beam hardening and was used to derive correction factors, which were then applied to projection data prior to reconstruction. To investigate the influence of the correction on the architecture and mineralization parameters, a second beam hardening correction based on a 1200 mg HA/cm^3 wedge phantom was also used.

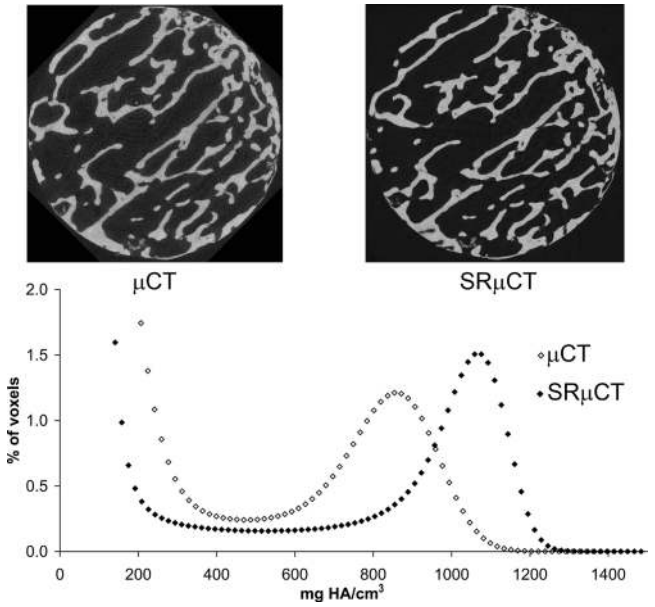

FIG. 1. Comparison of μCT and SRμCT images of a specimen from the human femoral head. Histograms of the two images are overlaid (background peaks truncated).

II.C. SRμCT imaging

SRμCT imaging was performed on beamline X2B of the National Synchrotron Light Source (Brookhaven National Laboratory, Upton, NY). This beamline is equipped with a monochromator to create a specific narrow energy incident beam. The collimated monochromatic beam passes through the sample, onto a cesium iodide scintillator, and is then projected through a 4× microscope objective onto a 16 bit CCD detector (2680×1300 pixels). The specimen holder is mounted on a computer-controlled high-precision rotation and translation stage.

The specimens were prepared for scanning by vacuum degassing in saline. All specimens were scanned under identical conditions using a 26 keV beam selected based on an established energy optimization protocol.[24,25] Each scan consisted of 1440 projections over 360 deg, with the sample rotated in equiangular steps about its longitudinal axis. For each projection, sampling occurred over an integration time of 1800–2200 ms (adjusted to compensate for beam decay over the beam fill cycle). Since the signal-to-noise ratio is high in SRμCT scans, a single projection was recorded per rotation. Dark current and raw beam measurements were made at intervals (every 20 or 40 projections, according to the beam decay profile) during each scan to adjust for detector inhomogeneities, spatial variation in beam intensity, and beam decay. Typical scanning time was 3–4 h per specimen. A filtered backprojection algorithm was applied to reconstruct 3D volume images with an isotropic voxel size of 7.50 μm.[26] The HA calibration phantom described above was scanned under the same conditions as the bone specimens and used to convert SRμCT grayscale values to HA concentration.

II.D. Image processing

All image processing steps were conducted using Image Processing Language (IPL, Scanco Medical AG) on an Alpha-based openVMS workstation (DS20E, Hewlett Packard, Inc.). Both μCT and SRμCT files were imported to the openVMS workstation as signed 16 bit data files. The SRμCT data were resampled to a voxel size of 8 μm. For both μCT and SRμCT data, contours encompassing the entire cross section of each slice were created semiautomatically to define the volume of interest (VOI) for analysis. A Gaussian filter (σ=1, 3×3 kernel) was applied to all images to remove high frequency noise. Thresholds were determined manually and verified through visual comparison to the original grayscale image. The threshold value most accurately delineating trabecular surfaces and voids in all specimens of a particular site and modality was chosen. The threshold selection for SRμCT images is straightforward due to the high contrast between tissue and background voxels. The μCT images have a lower signal-to-noise ratio and less well-resolved tissue and background histogram peaks and therefore require greater care in threshold selection (Fig. 1). A single threshold value was used for all specimens of a particular site and modality, therefore this technique is referred to as the fixed thresholding scheme. Thresholds were determined independently for SRμCT specimens (one threshold for each specimen type: FEM=715 mg HA/cm^3; TIB, VERT=556 mg HA/cm^3), for μCT with 200 mg HA/cm^3 correction (FEM=576 mg HA/cm^3; TIB, VERT=556 mg HA/cm^3), and for μCT with 1200 mg HA/cm^3 correction (FEM=576 mg HA/cm^3; TIB, VERT=556 mg HA/cm^3). Though they were independently selected, the thresholds were identical for the two

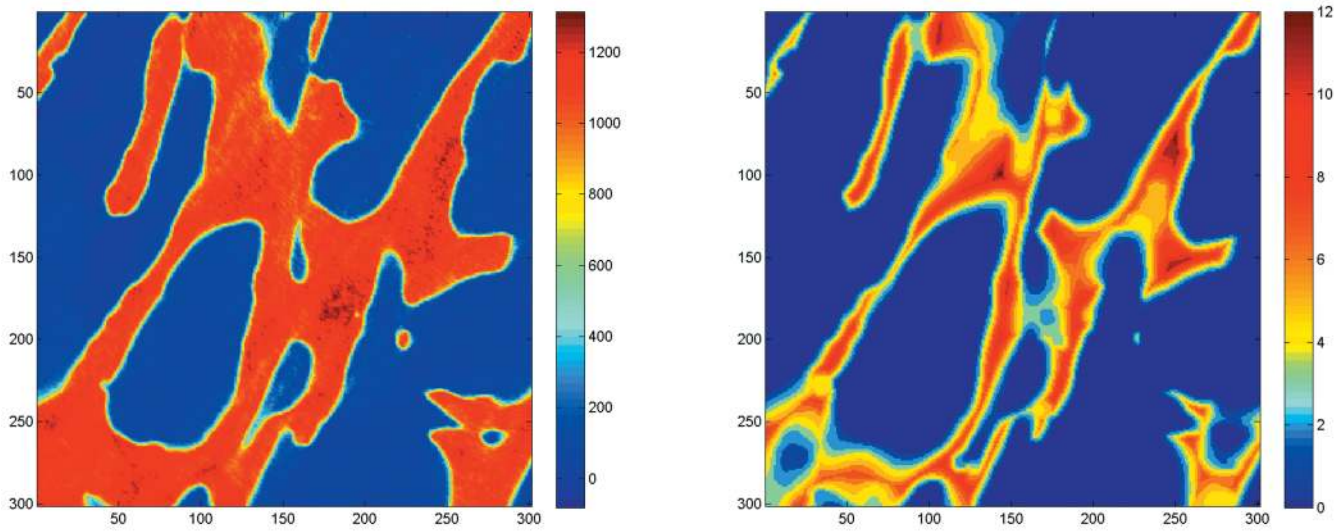

FIG. 2. Data representing mineralization and depth for each voxel within a portion of a SRμCT image. Left: Mineralization (mg HA/cm^3). Right: Distance from the nearest surface (voxels). Distance data are calculated in three dimensions.

μCT data sets. Similarly, thresholds for proximal tibia and vertebral specimens were identical within each group.

To investigate the influence of thresholding technique on the accuracy of μCT parameters, two additional thresholding schemes were applied to the μCT data with 200 mg HA/cm^3 correction. An adaptive thresholding scheme was applied, which automatically determined the grayscale value equivalent to the minimum change in bone volume fraction, or bone volume/total volume ratio (BV/TV). Additionally, a volume fraction matching approach was used, taking advantage of the ease of segmentation afforded by the high contrast SRμCT images. The volume fraction matching approach automatically determined an individual threshold for each μCT image by matching the resulting volume fraction to that of the associated SRμCT image.

II.E. Parameter evaluation

Structural parameters were calculated from the binarized reconstructions using code written in IPL. BV/TV was measured by direct voxel counting.[27] Trabecular thickness (Tb.Th), trabecular separation (Tb.Sp), and trabecular number (Tb.N) were calculated using a skeletonization routine and the model-independent 3D distance transform method.[28–30]

Mineralization parameters were calculated from the grey-level data using IPL and MATLAB (The Mathworks, Inc., Natick, MA) code. Based on the results of the thresholding technique investigation, the manually determined fixed thresholds were used for all of the following calculations. BMC and volume-averaged TMD for each specimen were calculated based on relationships derived from the rule of mixtures, which specifies that the mean density of a volume of interest is equal to the sum of the density of each component within the volume scaled by its volume fraction. For the case of trabecular bone with a uniform background this can be written as

$$\mathrm{TMD} = [\mathrm{BMD}_{\mathrm{VOI}} - \mathrm{BMD}_{\mathrm{back}} * (1 - \mathrm{BV/TV})]/(\mathrm{BV/TV}). \quad (1)$$

In this equation $\mathrm{BMD}_{\mathrm{VOI}}$ and $\mathrm{BMD}_{\mathrm{back}}$ are derived directly from the image data; $\mathrm{BMD}_{\mathrm{VOI}}$ is the mean mineralization value of all voxels in the VOI and $\mathrm{BMD}_{\mathrm{back}}$ is the mean mineralization of the background voxels. Prior to determining $\mathrm{BMD}_{\mathrm{back}}$ five voxels were eroded from the interface between bone and background to remove background voxels influenced by partial volume artifacts. By using this method to calculate TMD—rather than calculating the mean intensity of all bone voxels within a segmented image—we avoid the direct dependence of TMD on the number of voxels peeled from the bone surface.

BMC can be calculated by multiplying TMD by the total volume of bone in the imaged sample

$$\mathrm{BMC} = \mathrm{TMD}^{*}\mathrm{BV}. \quad (2)$$

To visualize the data in a spatially resolved manner, a distance value was assigned to each bone voxel in each data set (Fig. 2). This distance value represents the number of voxels separating the voxel in question from the nearest surface voxel. The average voxel mineralization was then calculated for each distance value within a given image. This allows the visualization of mineral distribution through the depth of the trabeculae. The same was done for the voxels in the interior of the cylinder (75% of the overall diameter) and for those in the outer periphery of the cylinder. To quantify the effects of beam hardening, geometric nonuniformity (cupping artifact) was assessed by comparing voxel intensities in the interior of the cylinder to those in the periphery. If a cupping artifact exists, we expect the mean mineralization value for the interior of the cylinder to be lower than that of the periphery for a given distance value. To calculate geometric nonuniformity, the difference between inner and peripheral voxel values was calculated at each distance value. Since surface voxels (lowest distance values) may be affected by partial

TABLE I. Regression statistics comparing architecture parameters calculated by μCT and SRμCT imaging. Three thresholding strategies (fixed, adaptive, volume fraction-matched) were implemented on μCT data with 200 mg/cm^3 beam hardening (BH) correction. Regression data for μCT data with 1200 mg/cm^3 BH correction (fixed threshold) is shown for comparison. All correlations significant at $p<0.0001$.

	μCT 200 BH vs SRμCT									μCT 1200 BH vs SRμCT		
	Fixed			Adaptive			VF-matched			Fixed		
	Slope	Int	R^2	Slope	Int	R^2	Slope	Int	R^2	Slope	Int	R^2
BV/TV	1.04	0.00	1.00	1.07	0.00	1.00	1.00	0.00	1.00	1.00	0.00	1.00
Tb.Th	0.98	0.01	1.00	1.08	−0.01	1.00	0.98	0.01	1.00	0.99	0.00	1.00
Tb.Sp	1.00	0.00	1.00	1.01	−0.01	1.00	1.01	0.00	1.00	1.02	−0.01	1.00
Tb.N	1.07	−0.07	0.99	1.07	−0.07	1.00	1.08	−0.08	0.99	1.08	−0.08	0.99

volume effects and voxels furthest from the surface (highest distance values) are not numerous enough to comprise a representative sample, they were excluded from this analysis.

II.F. Gravimetric analysis

Following μCT and SRμCT imaging, each specimen was processed using established gravimetric protocols.[11] Specimens were dehydrated in a furnace at 100 °C for 12 h, then ashed at 600 °C for 48 h. Ash mass was determined by weighing each specimen in its crucible once cooled back to room temperature, then subtracting the crucible weight determined prior to ashing. Measurements after an additional 24 h at 600 °C confirmed the complete removal of organic constituents. Ash density was calculated by dividing ash mass by tissue volume as measured by SRμCT imaging. This approach was deemed more accurate than relying on a water-displacement method for tissue volume measurement due to the ease of segmentation of SRμCT data. It also avoided potential physical damage to the specimens, which would have affected the ash mass measurement.

II.G. Statistics

Statistical computations were performed using JMP (SAS Institute, Inc., Cary NC). Residual analysis was performed to identify outliers. Results calculated from the μCT images using the two beam hardening corrections were compared using Wilcoxon sign-rank tests. The Friedman test was used to compare parameters obtained from μCT images using the two beam hardening corrections to those obtained via SRμCT imaging. Additional Friedman testing was used to compare μCT and SRμCT results to gravimetric measures. Comparisons between specimen groups (high versus low volume fraction groups) were performed using Wilcoxon sign-rank tests.

III. RESULTS

Specimens were divided into two volume fraction groups for comparisons among μCT, SRμCT, and gravimetric results: High volume fraction (HVF) including femur specimens (BV/TV=33±4) and low volume fraction (LVF) including tibia specimens (BV/TV=9±3) and vertebral specimens (BV/TV=9±3). One vertebral sample was identified as an outlier based on residual analysis of the mineralization data. On investigating the image data, we found that this sample contained small slivers of trabeculae created during the machining process. These slivers may have contributed to errors in mineralization data due to partial volume or segmentation artifacts. This sample was excluded from analysis.

III.A. Architecture

Regressions between μCT and SRμCT architecture parameters resulted in strong correlations for all threshold schemes and beam hardening corrections applied to the μCT images (Table I). Based on the comparison of regression statistics and in keeping with the literature[18,31] the fixed threshold scheme was chosen to be the basis of further analysis.

Differences in architecture values between the two μCT beam hardening corrections were small (Table II). In the HVF group, only Tb.Th was influenced by the beam hardening correction (1.5% diff; $p=0.008$). In the LVF group, all architecture parameters were influenced by changing the beam hardening correction (0.9% min diff, 5.1% max diff; $p=0.008$).

Small but significant differences between μCT and SRμCT data were found for all architecture parameters with the exception of Tb.Sp (Table II). Tb.Th values calculated by μCT were overestimated only with the 200 mg HA/cm^3 beam hardening correction (HVF 1.7%, LVF 2.5%). Tb.N values calculated by μCT were overestimated only in the HVF group (4.4% with both beam hardening corrections). BV/TV values calculated by μCT differed from SRμCT values only in the LVF group (1.1% overestimation with the 200 mg HA/cm^3 correction, 4.1% underestimation with the 1200 mg HA/cm^3 correction).

III.B. Mineralization

μCT-based BMC values were not affected by changing the beam hardening correction (Table II). TMD values in the HVF group were significantly different as calculated by the two beam hardening corrections ($p<0.0001$), with the 1200 mg HA/cm^3 beam hardening correction resulting in a 4.7% higher TMD value. In the LVF group there was no significant difference in TMD values calculated using the two beam hardening corrections.

TABLE II. Mean ± SD of architectural and mineralization parameters measured by μCT with 200 and 1200 mg/cm^3 BH corrections, SRμCT, and gravimetry. Specimens were divided into two groups for analysis: High volume fraction and low volume fraction.

	μCT						
	200BH	1200BH	200BH vs 1200BH[a]	SRμCT	μCT vs SRμCT [b]	Gravimetry	CT vs gravimetry[b]
High volume fraction: FEM (n=5)							
BV/TV (%)	33 ± 5	32 ± 4	NS	33 ± 4	NS	-	-
Tb.Th (μm)	191 ± 36	189 ± 36	0.008	188 ± 38	200BH	-	-
Tb.Sp (μm)	520 ± 61	523 ± 62	NS	520 ± 64	NS	-	-
Tb.N (1/mm)	1.9 ± 0.3	1.9 ± 0.3	NS	1.8 ± 0.3	200BH, 1200BH	-	-
BMC (mg)	68 ± 8	71 ± 9	NS	84 ± 10	200BH, 1200BH	91 ± 11	200BH, 1200BH, SR
TMD (mg HA/cm^3)	942 ± 24	987 ± 24	0.008	1147 ± 24	200BH, 1200BH	1251 ± 51	200BH, 1200BH, SR
Low volume fraction: TIB (n=4) and VERT (n=4)							
BV/TV (%)	9 ± 3	9 ± 3	0.008	9 ± 3	200BH, 1200BH	-	-
Tb.Th (μm)	126 ± 16	123 ± 16	0.008	123 ± 16	200BH	-	-
Tb.Sp (μm)	958 ± 174	969 ± 177	0.008	952 ± 172	NS	-	-
Tb.N (1/mm)	1.0 ± 0.2	1.0 ± 0.2	0.008	1.0 ± 0.2	NS	-	-
BMC (mg)	19 ± 7	19 ± 7	NS	22 ± 8	200BH, 1200BH	25 ± 8	200BH, 1200BH, SR
TMD (mg HA/cm^3)	1027 ± 27	1023 ± 23	NS	1161 ± 30	200BH, 1200BH	1295 ± 36	200BH, 1200BH, SR

[a]p values based on Wilcoxon signed-rank tests. NS indicates no significant difference.
[b]μCT measurements statistically different from SRμCT, and tomography measurements statistically different from gravimetry are listed ($p<0.05$ Friedman tests). NS indicates no significant differences were found between μCT (either beam hardening correction) and SRμCT.

Significant differences between μCT and SRμCT mineralization values were found in both volume fraction groups (Table II). In the HVF group, the 1200 mg HA/cm^3 correction resulted in BMC and TMD values 16.7% and 15.0% lower, respectively, than SRμCT values. In the LVF group, the 1200 mg HA/cm^3 correction resulted in BMC and TMD values 12.8% and 12.9% lower, respectively, than SRμCT values.

The relatively larger underestimation of mineralization measures in HVF bone led to a further discrepancy between μCT and SRμCT data; in the μCT data set TMD of the HVF group was significantly lower than that of the LVF group (p=0.004), while in the SRμCT analysis the groups had statistically indistinguishable TMD values.

Gravimetric ash mass and density were significantly higher than SRμCT (and consequently μCT) mineralization values in both volume fraction groups (Table II). In the HVF group, both ash mass and ash density were higher than the SRμCT equivalents by 8.6%. In the LVF group, ash mass and ash density were higher than the SRμCT equivalents by 10.9%.

Individual specimen values as well as regressions were plotted to explore relationships among μCT, SRμCT, and gravimetry mineralization results (Fig. 3). BMC values calculated by tomography were highly correlated with ash mass (ash versus μCT R^2=0.96–1.00; ash versus SRμCT R^2=0.99–1.00). High correlations were found between μCT and SRμCT BMC values (R^2=0.97–1.00). Though no significant differences were found between μCT BMC values calculated using the two beam hardening corrections, the 1200 mg HA/cm^3 correction consistently yielded results closer to the SRμCT values.

TMD values calculated by tomography were moderately correlated with ash density (ash versus μCT R^2=0.64–0.72; ash versus SRμCT R^2=0.64). Of the two μCT beam hardening algorithms the 200 mg HA/cm^3 correction had a greater slope when regressed against ash density, resulting from beam hardening in the HVF samples. With the 1200 mg HA/cm^3 correction the measured tissue density of the HVF samples increased resulting in a slope almost equal to that of the SRμCT regression (Fig. 3). μCT and SRμCT TMD values were well correlated with each other when volume fraction groups were considered individually (HVF R^2=0.90–0.99; LVF R^2=0.78). With the 200 mg HA/cm^3 correction, μCT-derived TMD of the HVF group was lower than that of the LVF group, with similar slope. The 1200 mg HA/cm^3 correction moved the HVF group toward the LVF regression, softening the dependence on volume fraction.

To ensure that thresholding technique did not influence our results, BMC and TMD were recalculated for the μCT data using the adaptive and volume fraction matching thresholding schemes (results not shown). These alternative schemes resulted in slight shifts of absolute TMD and BMC values, however, the tomography versus ash and μCT versus SRμCT regressions were similar to the results of the fixed threshold scheme shown in Fig. 3.

Spatially resolved comparisons highlighted substantial geometric nonuniformity in the μCT data that did not exist in the SRμCT data (Figs. 4 and 5). Geometric nonuniformity was quantified as the discrepancy between mineralization values of the voxels in the inner and peripheral regions of the specimen cylinder. For every specimen, the μCT data with 200 mg HA/cm^3 correction produced the greatest discrepancy in mineralization values. The discrepancy was most extreme in the HVF samples (mean diff between inner and peripheral mineralization=46.7 ± 3.3 mg HA/cm^3). The 1200 mg HA/cm^3 correction lessened the discrepancy be-

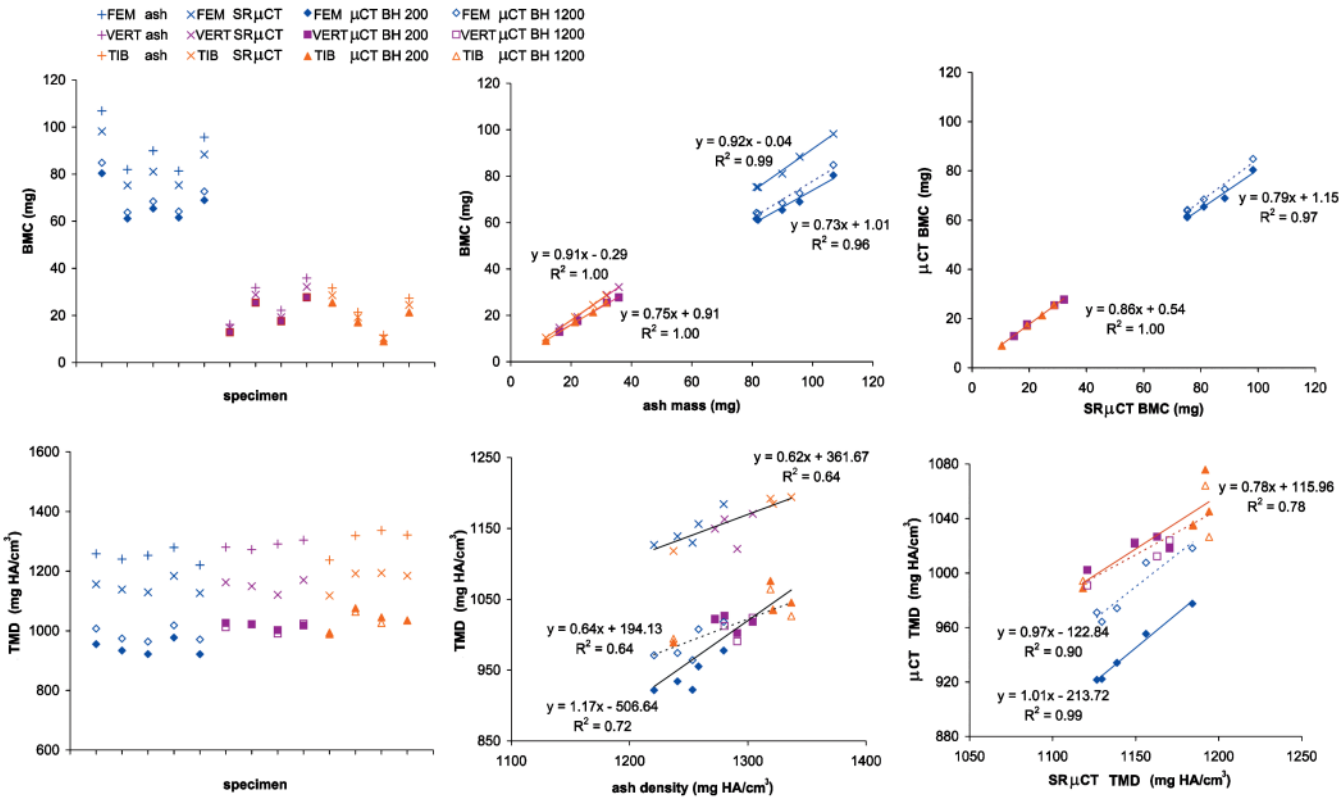

FIG. 3. Left column: BMC and TMD values as measured by gravimetry (+), SRμCT ($\times$), μCT with 200 mg HA/cm^3 BH correction (closed symbols, solid lines), and μCT with 1200 mg HA/cm^3 BH correction (open symbols, dotted lines). Middle column: Regressions of BMC vs ash mass and TMD vs ash density. Right column: Regressions of μCT BMC vs SRμCT BMC and μCT TMD vs SRμCT TMD. All regressions significant at $p<0.0001$.

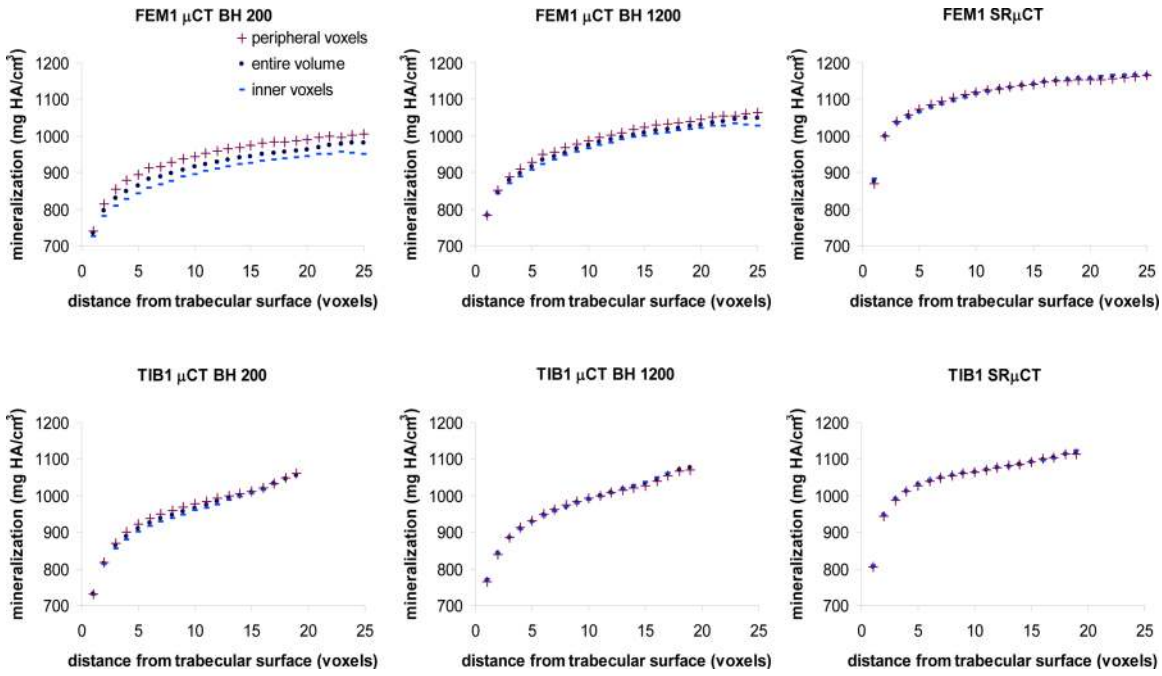

FIG. 4. Visualization of mineral density as a function of distance from trabecular surface. Mean mineralization was calculated at each distance value for all voxels (circles), for those in the interior of the specimen only (dashes), and for those in the outer periphery only (pluses). The discrepancy between the inner and peripheral regions was used to quantify geometric nonuniformity (cupping artifact). The greatest discrepancy occurred in high volume fraction bone imaged on the μCT with the 200 mg HA/cm^3 correction (top left). The 1200 mg HA/cm^3 correction reduced this discrepancy (top middle), and the SRμCT data revealed no discrepancy (top right). The effect was less evident in low volume fraction bone (bottom row).

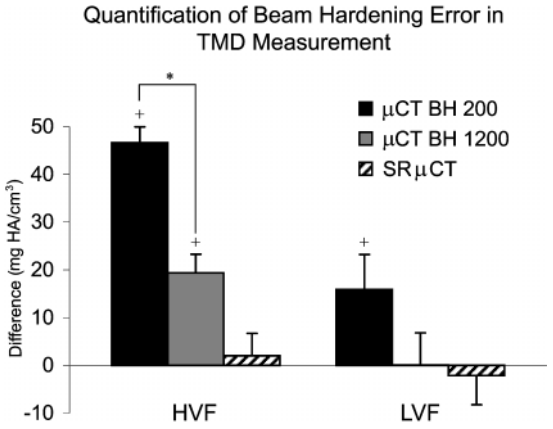

FIG. 5. Quantification of geometric nonuniformity resulting from beam hardening artifact. Values represent discrepancy in mineralization values between peripheral and central voxels. Results for high volume fraction (HVF) and low volume fraction (LVF) groups are displayed individually. + denotes significant difference from zero ($p<0.0001$). ∗ denotes significant difference between nonzero groups.

tween inner and outer regions (mean diff $=19.4\pm3.9$ mg HA/cm^3). The synchrotron values showed no discrepancy.

IV. DISCUSSION

Our results indicate that μCT mineralization measures are underestimated but well correlated with SRμCT and gravimetric data, particularly when structure types (specifically volume fraction groups) are considered individually. Evidence of beam hardening artifact was found in both high and low volume fraction bone despite the use of a beam hardening correction algorithm based on a 200 mg HA/cm^3 wedge phantom. In HVF specimens beam hardening artifacts caused geometric nonuniformity in mineralization values of substantial amplitude, approximately 50 mg HA/cm^3 or 60% of the range of TMD across the sample population. Geometric nonuniformity and TMD underestimation was reduced by employing a correction algorithm based on a 1200 mg HA/cm^3 phantom; however, evidence of beam hardening was still present in HVF bone, indicating the need for a more effective beam hardening correction in some cases.

The primary strength of this study is the use of SRμCT as the gold standard for quantitative comparison. The monochromatic beam precludes beam hardening; at our scanning energy of 26 keV the bandwidth is on the order of 5 eV, which would produce a variation of less than 0.1% in linear attenuation. The beam is highly collimated, eliminating the need for cone beam approximations in the reconstruction algorithm. High flux ensures excellent signal-to-noise characteristics. A second strength of this study is the use of trabecular bone samples spanning a range of structure types. By dividing our samples into groups based on volume fraction we were able to discern and quantify the volume fraction-dependence of beam hardening effects. Finally, this study compared two beam hardening correction algorithms, quantifying the beam hardening artifact extant with each. A limitation of this work is the use of a single μCT system. Systems supplied by other manufacturers may be subject to different errors and artifacts as they employ unique hardware, source voltage, beam filters, and software artifact corrections.[32] Thickness and density of the beam filter in particular may influence beam hardening artifacts by altering the energy spectrum of the beam. Though results are specific to the μCT 40 system, the points of caution drawn from our comparison are applicable to all polychromatic systems.

The results presented here were determined using TMD calculated from Eq. (2). An alternative approach would be to calculate TMD as the mean intensity of all voxels representing bone. This method would require a segmentation step to identify bone voxels followed by erosion of surface voxels to avoid partial volume artifacts. TMD values calculated in this way are highly sensitive to surface voxel erosion, while TMD derived from Eq. (2) avoids this dependence on voxel erosion. Data analysis was repeated for TMD calculated from the mean intensity of bone voxels (results not shown). The resulting relationships between tomography and ash were weaker than those shown here, and relationships between μCT and SRμCT were slightly stronger. TMD values were 8% lower than those reported here ($p<0.0001$).

This study found increased accuracy and decreased cupping artifact with the 1200 mg HA/cm^3 correction, confirming the recommendation previously made based on idealized phantom imaging.[33] This finding suggests that density of the wedge phantom used to produce the correction factor should be chosen based on maximum tissue density rather than mean apparent density of the specimen, as has been a common approach in the past.

Though evidence of beam hardening was reduced—or in the case of LVF bone, eliminated—by the 1200 mg HA/cm^3 correction, TMD was still significantly underestimated suggesting the presence of additional sources of error. The mineralization phantom may be one important source of this error. The mineralization phantom contains density regions of 0–800 mg HA/cm^3. Because the majority of voxels within adult human bone specimens are at a mineralization level greater than 800 mg HA/cm^3, extrapolation of the calibration curve is necessary to convert attenuation to HA concentration. As beam hardening artifacts will also exist in the phantom scan and are clearly dependant on density, it is possible that extrapolation causes errors in the calculation of high intensity voxels.[34] Recently, methods have been proposed to manufacture pure HA-based phantoms with concentrations up to 3 g/cm^3, which may be employed in the future to avoid the need for extrapolation in performing calibrations.[34]

Ash values (mass and density) were significantly higher than the μCT and SRμCT equivalents. Previous validation of tomographic mineral density quantification is limited to comparisons between SRμCT and microradiograph TMD; relative error comparing the two techniques ranges from 2.2% to 6.5%.[20] It is expected that error between two x-ray based techniques would be smaller than that between tomog-

raphic and gravimetric techniques. Some portion of the discrepancy between tomography and gravimetry seen in this study may be related to our method of calculating ash density, which uses tissue volume calculated by SRμCT as opposed to that directly measured from the sample using Archimedes principle. It is possible that the tissue volume calculated by SRμCT is underestimated—organic material or osteoid surfaces may be excluded by the segmentation process. It is also possible that ash mass includes components—those of the nonstoichometric HA found in bone, for example—which are not adequately accounted for by the HA phantom calibration.[35] Though steps were taken to prevent sample rehydration prior to measurement of ash mass, such rehydration may be another source of discrepancy between ash and tomographic values. TMD values calculated by μCT (with the 1200 mg HA/cm^3 correction) and SRμCT and are related to ash density with similar slopes that are far less than one (Fig. 3). It is possible that the effects described above are volume fraction-dependant in a manner that would cause this relationship. Compton or other scatter phenomena may also influence attenuation measurements in a volume fraction-dependant manner, contributing to this relationship.

This study represents the first quantitative comparison of μCT mineralization evaluation against SRμCT and gravimetry. Our findings are significant in the context of mineralization assessment of human biopsies, animal models, and tissue engineered bone using polychromatic μCT systems. These studies often include specimens of varying architecture and volume fraction, and therefore may be subject to errors due to artifacts that may mask effects of experimental treatments. The interaction between volume fraction and beam hardening artifact must be considered when investigating specimens from different subjects or anatomical sites, or when comparing different regions within one scan. Additional work is necessary to investigate more appropriate mineralization calibrations, to devise more robust beam hardening correction algorithms, and to isolate possible volume fraction-dependant errors.

ACKNOWLEDGMENTS

The authors would like to acknowledge the generous contributions of Steve Jorgensen, John Dunsmuir, Tony Keaveny, Andres Laib, and Sven Prevrhal to this work. This research was supported by NIH F32 AR053446.

[a]Present address: 1700 4th Street, Suite 203, San Francisco, CA 94158. Telephone: 415-514-9663; Fax: 415-514-9656. Electronic mail: galateia.kazakia@radiology.ucsf.edu

[1]M. Kleerekoper, A. R. Villanueva, J. Stanciu, D. S. Rao, and A. M. Parfitt, "The role of three-dimensional trabecular microstructure in the pathogenesis of vertebral compression fractures," Calcif. Tissue Int. **37**, 594–597 (1985).

[2]M. J. Ciarelli, S. A. Goldstein, J. L. Kuhn, D. D. Cody, and M. B. Brown, "Evaluation of orthogonal mechanical properties and density of human trabecular bone from the major metaphyseal regions with materials testing and computed tomography," J. Orthop. Res. **9**, 674–682 (1991).

[3]B. L. Riggs and L. J. Melton III, "Bone turnover matters: The raloxifene treatment paradox of dramatic decreases in vertebral fractures without commensurate increases in bone density," J. Bone Miner. Res. **17**, 11–14 (2002).

[4]C. L. Gordon, T. F. Lang, P. Augat, and H. K. Genant, "Image-based assessment of spinal trabecular bone structure from high-resolution CT images," Osteoporos. Int. **8**, 317–325 (1998).

[5]C. H. Chesnut III and C. J. Rosen, "Reconsidering the effects of antiresorptive therapies in reducing osteoporotic fracture," J. Bone Miner. Res. **16**, 2163–2172 (2001).

[6]J. Y. Rho, P. Zioupos, J. D. Currey, and G. M. Pharr, "Variations in the individual thick lamellar properties within osteons by nanoindentation," Bone **25**, 295–300 (1999).

[7]A. C. Courtney, W. C. Hayes, and L. J. Gibson, "Age-related differences in post-yield damage in human cortical bone. Experiment and model," J. Biomech. **29**, 1463–1471 (1996).

[8]T. M. Boyce and R. D. Bloebaum, "Cortical aging differences and fracture implications for the human femoral neck," Bone **14**, 769–778 (1993).

[9]M. J. Jaasma, H. H. Bayraktar, G. L. Niebur, and T. M. Keaveny, "Biomechanical effects of intraspecimen variations in tissue modulus for trabecular bone," J. Biomech. **35**, 237–246 (2002).

[10]P. J. Meunier and G. Boivin, "Bone mineral density reflects bone mass but also the degree of mineralization of bone: Therapeutic implications," Bone **21**, 373–377 (1997).

[11]J. Galante, W. Rostoker, and R. D. Ray, "Physical properties of trabecular bone," Calcif. Tissue Res. **5**, 236–246 (1970).

[12]G. Boivin and P. J. Meunier, "The degree of mineralization of bone tissue measured by computerized quantitative contact microradiography," Calcif. Tissue Int. **70**, 503–511 (2002).

[13]R. D. Bloebaum, J. G. Skedros, E. G. Vajda, K. N. Bachus, and B. R. Constantz, "Determining mineral content variations in bone using backscattered electron imaging," Bone **20**, 485–490 (1997).

[14]P. K. Zysset, X. E. Guo, C. E. Hoffler, K. E. Moore, and S. A. Goldstein, "Elastic modulus and hardness of cortical and trabecular bone lamellae measured by nanoindentation in the human femur," J. Biomech. **32**, 1005–1012 (1999).

[15]L. F. Bonewald, S. E. Harris, J. Rosser, M. R. Dallas, S. L. Dallas, N. P. Camacho, B. Boyan, and A. Boskey, "von Kossa staining alone is not sufficient to confirm that mineralization *in vitro* represents bone formation," Calcif. Tissue Int. **72**, 537–547 (2003).

[16]B. Borah, E. L. Ritman, T. E. Dufresne, S. M. Jorgensen, S. Liu, J. Sacha, R. J. Phipps, and R. T. Turner, "The effect of risedronate on bone mineralization as measured by micro-computed tomography with synchrotron radiation: Correlation to histomorphometric indices of turnover," Bone **37**, 1–9 (2005).

[17]F. Peyrin, M. Salome, S. Nuzzo, P. Cloetens, A. M. Laval-Jeantet, and J. Baruchel, "Perspectives in three-dimensional analysis of bone samples using synchrotron radiation microtomography," Cell. Mol. Biol. (Paris) **46**, 1089–1102 (2000).

[18]C. Chappard, A. Basillais, L. Benhamou, A. Bonassie, B. Brunet-Imbault, N. Bonnet, and F. Peyrin, "Comparison of synchrotron radiation and conventional x-ray microcomputed tomography for assessing trabecular bone microarchitecture of human femoral heads," Med. Phys. **33**, 3568–3577 (2006).

[19]L. Mulder, J. H. Koolstra, and T. M. Van Eijden, "Accuracy of microCT in the quantitative determination of the degree and distribution of mineralization in developing bone," Acta Radiol. **45**, 769–777 (2004).

[20]S. Nuzzo, F. Peyrin, P. Cloetens, J. Baruchel, and G. Boivin, "Quantification of the degree of mineralization of bone in three dimensions using synchrotron radiation microtomography," Med. Phys. **29**, 2672–2681 (2002).

[21]M. Ito, S. Ejiri, H. Jinnai, J. Kono, S. Ikeda, A. Nishida, K. Uesugi, N. Yagi, M. Tanaka, and K. Hayashi, "Bone structure and mineralization demonstrated using synchrotron radiation computed tomography (SR-μCT) in animal models: Preliminary findings," J. Bone Miner. Metab. **21**, 287–293 (2003).

[22]P. Ruegsegger, B. Koller, and R. Müller, "A microtomographic system for the nondestructive evaluation of bone architecture," Calcif. Tissue Int. **58**, 24–29 (1996).

[23]L. A. Feldkamp, S. A. Goldstein, A. M. Parfitt, G. Jesion, and M. Kleerekoper, "The direct examination of three-dimensional bone architecture *in vitro* by computed tomography," J. Bone Miner. Res. **4**, 3–11 (1989).

[24]L. Grodzins, "Optimum energies for x-ray transmission tomography of small samples: Applications of synchrotron radiation to computerized tomography I," Nucl. Instrum. Methods Phys. Res. **206**, 541–545 (1983).

[25]S. M. Jorgensen, O. Demirkaya, and E. L. Ritman, "Three-dimensional imaging of vasculature and parenchyma in intact rodent organs with x-ray micro-CT," Am. J. Physiol. **275**, H1103–H1114 (1998).
[26]E. L. Ritman, S. M. Jorgensen, P. E. Lund, P. J. Thomas, J. H. Dunsmuir, J. C. Romero, R. T. Turner, and M. E. Bolander, "Synchrotron-based micro-CT of *in situ* biological basic functional units and their integration," SPIE Dev. X-Ray Tomography **3149**, 13–24 (1997).
[27]M. Ding, A. Odgaard, and I. Hvid, "Accuracy of cancellous bone volume fraction measured by micro-CT scanning," J. Biomech. **32**, 323–326 (1999).
[28]T. Hildebrand and P. Rüegsegger, "A new method for the model-independent assessment of thickness in three-dimensional images," J. Microsc. **185**, 67–75 (1997).
[29]A. Laib, T. Hildebrand, H. J. Hauselmann, and P. Ruegsegger, "Ridge number density: A new parameter for *in vivo* bone structure analysis," Bone **21**, 541–546 (1997).
[30]R. Muller, T. Hildebrand, and P. Ruegsegger, "Non-invasive bone biopsy: A new method to analyse and display the three-dimensional structure of trabecular bone," Phys. Med. Biol. **39**, 145–164 (1994).
[31]R. Müller, H. Van Campenhout, B. Van Damme, G. Van Der Perre, J. Dequeker, T. Hildebrand, and P. Ruegsegger, "Morphometric analysis of human bone biopsies: A quantitative structural comparison of histological sections and micro-computed tomography," Bone **23**, 59–66 (1998).
[32]A. J. Olejniczak, P. Tafforeau, T. M. Smith, H. Temming, and J. J. Hublin, "Technical note: Compatibility of microtomographic imaging systems for dental measurements," Am. J. Phys. Anthropol. **134**, 130–134 (2007).
[33]R. Fajardo, E. Cory, N. Patel, A. Nazarian, B. Snyder, and M. L. Bouxsein, *Specimen Size and Porosity Can Introduce Error Into mCT-Based Tissue Mineral Density Measurements* (Orthopaedic Research Society, San Diego, CA, 2007).
[34]S. Schweizer, B. Hattendorf, P. Schneider, B. Aeschlimann, L. Gauckler, R. Muller, and D. Gunther, "Preparation and characterization of calibration standards for bone density determination by micro-computed tomography," Analyst (Cambridge, U.K.) **132**, 1040–1045 (2007).
[35]A. A. Postnov, A. V. Vinogradov, D. Van Dyck, S. V. Saveliev, and N. M. De Clerck, "Quantitative analysis of bone mineral content by x-ray microtomography," Physiol. Meas. **24**, 165–178 (2003).